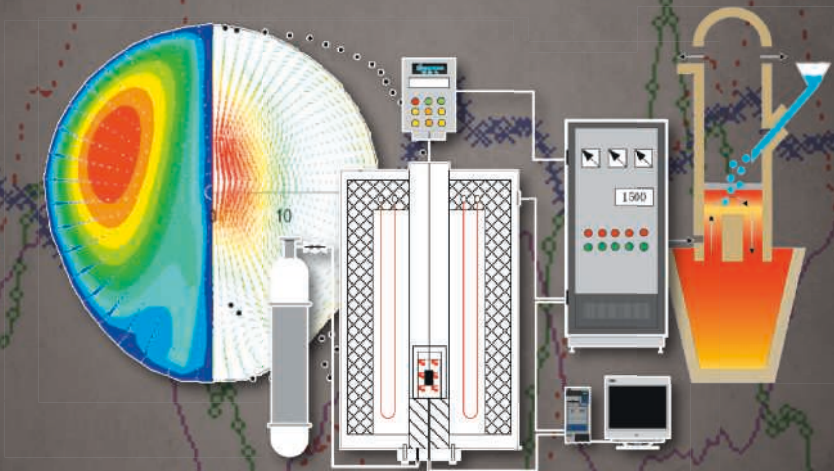# MATERIALS PROCESSING
## FUNDAMENTALS 2021

EDITED BY

Jonghyun Lee
Samuel Wagstaff
Alexandra Anderson
Fiseha Tesfaye
Guillaume Lambotte
Antoine Allanore

TMS

△ Springer

# The Minerals, Metals & Materials Series

Jonghyun Lee · Samuel Wagstaff ·
Alexandra Anderson · Fiseha Tesfaye ·
Guillaume Lambotte · Antoine Allanore
Editors

# Materials Processing Fundamentals 2021

**TMS**

 Springer

*Editors*
Jonghyun Lee
Iowa State University
Ames, IA, USA

Samuel Wagstaff
Oculatus
Marietta, GA, USA

Alexandra Anderson
Gopher Resource
Tampa, FL, USA

Fiseha Tesfaye
Åbo Akademi University
Turku, Finland

Guillaume Lambotte
Boston Metal
Woburn, MA, USA

Antoine Allanore
Massachusetts Institute of Technology
Cambridge, MA, USA

Cover Illustration: Left: From Chapter "Containerless Materials Processing for Materials Science on Earth and in Space", Jonghyun Lee et al., Figure 3: Left [33]: Convection velocity field in an EM-levitated Co–Cu droplet. Black dots indicate surface convection velocity along the meridian. Convection velocity near the equator is predicted as $\sim 30$ cm·s$^{-1}$; middle [37]: numerically predicted maximum convection velocity as a function of heater current in a Fe–Co droplet processed using the ISS-EML; right [31]: predicted accessible range of convection (gray parallelogram) in a Fe–Co sample during ISS-EML processing. https://doi.org/10.1007/978-3-030-65253-1_16. Middle: From Chapter "Influence of Cr$_2$O$_3$ Content on Phase of Chromium-Containing High-Titanium Blast Furnace Slag", Ding Yang et al., Figure 1: Experimental apparatus for the slag viscosity measurements. https://doi.org/10.1007/978-3-030-65253-1_19. Right: From Chapter "Study on Evolution of Inclusions in Tinplate Production During RH Refining—Continuous Casting Process", Xiaoao Li et al., Figure 1: Illustration of sampling during RH refining process. https://doi.org/10.1007/978-3-030-65253-1_5.

# Preface

The symposium Materials Processing Fundamentals is hosted at the Annual Meeting of The Minerals, Metals & Materials Society (TMS) as the flagship symposium of the Process Technology and Modeling Committee. It is a unique opportunity for interdisciplinary presentations and discussions about, among others, processing, sensing, modeling, multi-physics, computational fluid dynamics, and thermodynamics.

The materials covered include ferrous and non-ferrous elements, and the processes range from mining unit operations to jointing and surface finishing of materials. Acknowledging that modern processes involve multi-physics, the symposium and its proceedings allow the reader to learn the methods and outcome of other fields' modeling practices, often enabling the development of practical solutions to common problems. Modeling of basic thermodynamic and physical properties plays a key role, along with computational fluid dynamics and multi-phase transport and interface modeling.

Contributions to the proceedings include applications such as steel processing, modeling of steel and non-ferrous alloys treatments for properties control, multi-physics and computational fluid dynamics modeling for molten metal processes and properties measurement. Extractive, recovery, and recycling process modeling is also presented, completing a broad view of the field and practices of modeling in materials processing.

The engagement of TMS and committee members to chair sessions and review manuscripts makes this symposium and its proceedings possible. The editor and co-editors acknowledge the invaluable support and contribution of these volunteers as well as TMS staff members, in particular, Patricia Warren, Trudi Dunlap, and Matt Baker.

<div align="right">
Jonghyun Lee<br>
Samuel Wagstaff<br>
Alexandra Anderson<br>
Fiseha Tesfaye<br>
Guillaume Lambotte<br>
Antoine Allanore
</div>

# Contents

# About the Editors

**Jonghyun Lee** is an assistant professor in the Department of Mechanical Engineering at Iowa State University. He has been conducting multiple industry and government-funded projects in the field of materials processing as PI and Co-PI. He is the recipient of the Young Leaders Professional Development Award in 2013 from The Minerals, Metals & Materials Society where he has been serving as a co-organizer and co-editor of the Materials Processing Fundamentals Symposium since 2014 and as chair of the Process Technology and Modeling Committee since 2019. Prior to joining his current institution, he was a research assistant professor at the University of Massachusetts, Amherst. He also had nearly 5 years of industry experience and worked as a postdoctoral associate for Tufts University, Medford, Massachusetts. He earned his M.S. and Ph.D. in Mechanical Engineering from the University of Massachusetts Amherst and his B.S. in the same discipline from Inha University in Incheon, South Korea.

**Samuel Wagstaff** is currently a partner at Oculatus Consulting, specializing in aluminum processing and product development. He earned his B.Sc. degree from Cornell University in Mechanical and Aerospace Engineering in 2013. He earned a M.Sc. degree at the Massachusetts Institute of Technology focusing on characterizing macrosegregation patterns in large format rolling slabs. He then earned a Sc.D. in 2016 also from MIT for his work on engineering convective flows to minimize the appearance of macrosegregation. Following his graduate studies, he worked at Novelis in their rolling facility in Sierre, Switzerland in their automotive development department, focusing on process refinement and product troubleshooting. In 2018 he moved to the Novelis R&D center in Kennesaw, Georgia where he became a lead scientist for product and process development. At Oculatus, he works on next-generation technologies for the aluminum sector and improvements in current processes. His current focus is on improving the profitability of existing centers via casting process improvement and recycle-based product development. Dr. Wagstaff is the author of 16 peer-reviewed articles, and inventor of over 25 patent applications.

**Alexandra Anderson** is a senior research and development engineer at Gopher Resource, a lead battery recycler, in Tampa, Florida. She received her Bachelor of Science degree in Mechanical Engineering from Gonzaga University in 2013, continuing her education at the Colorado School of Mines where she earned both a Master of Science and a Doctor of Philosophy in Metallurgical and Materials Engineering. Her doctoral research focused on computational fluid-dynamic modeling of reverberatory furnaces use for secondary lead production. At Gopher Resource, Alexandra directs the reverberatory furnace productivity program, encompassing all optimization and expansion projects related to the furnace as well as burner technology implementation and computational modeling initiatives. Dr. Anderson is an active TMS volunteer, serving as

secretary of both the Process Technology and Modeling Committee and the Recycling and Environmental Technologies Committee.

**Fiseha Tesfaye** is a senior researcher with the title of Docent in metallurgical thermodynamics in the Johan Gadolin Process Chemistry Centre of Åbo Akademi University, Finland. He received his M.Sc. degree in materials processing technology and Ph.D. degree in metallurgy from Aalto University, Finland. His research activities are focused mainly on the thermodynamic investigation of inorganic materials as well as rigorous theoretical and experimental investigations for promoting improved valuable metals and renewable energy production. In 2018, Dr. Tesfaye was also appointed as a visiting research scientist in Seoul National University, South Korea.

Dr. Tesfaye is a regular contributor and active member of The Minerals, Metals & Materials Society (TMS), and is a winner of the 2018 TMS Young Leaders Professional Development Award. He serves as a subject editor for *JOM*, the member journal of TMS, and has edited several scientific research books. His personal research achievements include remarkable improvement of experimental research applying the solid-state EMF technique for thermodynamic investigations of inorganic materials, as well as noticeable contribution for promoting the move toward the circular economy. In his research areas, Dr. Tesfaye has published over 55 peer-reviewed publications.

**Guillaume Lambotte** is the VP of Research and Development at Boston Metal, a Massachusetts Institute of Technology (MIT) spin-off startup focusing on the development of an environmentally friendly and energetically efficient primary metal extraction process. Dr. Lambotte primarily focuses on computational thermodynamic modeling, electrochemistry, and high-temperature equilibrium. Prior to joining Boston Metal, he conducted research as a post-doctoral associate at the University of Massachusetts Amherst and MIT. Before his graduate studies, Dr. Lambotte worked as a production assistant manager at Alcan Extruded Products (Crailsheim, Germany).

Dr. Lambotte obtained his bachelor's degree from the European Engineer School for Materials Science (Nancy, France). He received a M.Sc. and a Ph.D. in metallurgical engineering from Ecole Polytechnique of Montreal (Montreal, Canada).

Dr. Lambotte was the recipient of the 2015 TMS EPD Young Leaders Professional Development Award. The same year he was one of the TMS representatives at the Emerging Leaders Alliance Conference.
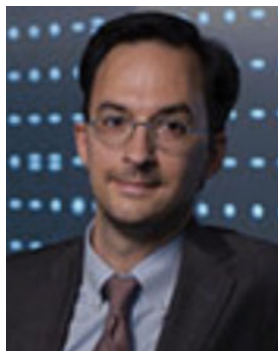


**Antoine Allanore** is an associate professor of metallurgy in the Department of Materials Science and Engineering at MIT. He received his higher education in Nancy (France) where he earned a chemical process engineer diploma from Ecole Nationale Supérieure des Industries Chimiques and a M.Sc. and Ph.D. from Lorraine University. Dr. Allanore joined MIT in 2012 as a faculty member, leading a research group that develops sustainable materials extraction and manufacturing processes. He has developed numerous alternative approaches for metals and minerals extraction and processing. With an emphasis on electrochemical methods for both analytical and processing purposes, his group combines experimental and modeling approaches to promptly investigate the ultimate state of condensed matter, the molten state. He teaches thermodynamics and sustainable chemical metallurgy at both the undergraduate and graduate levels. He received the Vittorio de Nora Award from TMS in 2012, and the TMS Early Career Faculty Fellow Award in 2015.

# Part I
# Molten Metal Processing and Modeling

# Effect of Turbulence Suppressor on Molten Steel Flow in Tundish

**Jie Luo, Si-kun Peng, Ai-ping Zhang, and Yong Zhong**

**Abstract** In this paper, the influence of the structure of turbulence inhibitor on the flow of molten steel in tundish is studied. By means of numerical simulation, by changing the shape of turbulence inhibitor and adding eaves on the top, the different influences on the flow field, temperature field, inclusion removal rate, molten steel quality, and residence time distribution curve of the whole tundish and the injection zone are obtained. By comparing the effects of four different shapes of turbulence inhibitors, this paper provides guidance for the design of flow control device in tundish.

**Keywords** Turbulence suppressor · Numerical simulation · Flow field · Temperature field

## Introduction

As a fluid reactor, tundish plays an important role in the continuous casting process. The molten steel from the ladle flows to the tundish through the long nozzle and flows to the mold through the tundish to achieve the purpose of continuous casting. The flow mode and residence time of molten steel in tundish will affect the flow mode of molten steel and the floating of inclusions, which are closely related to the quality of continuous casting billet [1–4]. Therefore, setting reasonable flow control device in tundish is an important way to optimize the flow mode and mixing uniformity of molten steel in tundish. In recent years, turbulence inhibitors have been widely used. Turbulence inhibitors have different shapes. Their outer wall size and structure are of great significance to the flow pattern of molten steel in tundish.

He et al. [5] pointed out that the effect of circular turbulence inhibitor on the flow characteristics of molten steel in the impact zone is very obvious. It can improve the mixing ability of molten steel, promote the collision, growth, and removal of non-metallic inclusions, promote the homogenization of temperature and composition

J. Luo (✉) · S. Peng · A. Zhang · Y. Zhong
College of Materials Science and Engineering, Chongqing University, Chongqing 400044, China
e-mail: 201909131200@cqu.edu.cn

of molten steel, and prevent the erosion of tundish lining in impact zone by high-speed molten steel. Yang et al. [6] found that in asymmetric double-flow tundish, the temperature difference between two outlets can be effectively reduced by using asymmetric turbulence inhibitor and wall with guide hole. Merder [7] found that turbulence inhibitors have a favorable effect on the durability of refractory lining near the inlet zone; compared with tundish without turbulence inhibitors, the application of turbulence inhibitors makes the mixing of molten steel better. This improvement is based on increasing the dynamics of molten steel mixing, so that the centralized mixing zone of molten steel is also larger. This situation is conducive to floating non-metallic inclusions into the slag.

To sum up, in order to obtain the ideal flow mode and mixing degree of molten steel in tundish and improve the impurity removal rate, this paper takes the rectangular large capacity tundish as the research object, carries on the numerical simulation for several different turbulence inhibitors in the injection area, compares with the original tundish, and concludes that the influence of turbulence inhibitors with different shapes and structures on the molten steel flow is in the injection zone. Finally, it provides guidance for designing reasonable turbulence inhibitor in large capacity tundish.

## Numerical Simulation Research Method

### Model Hypothesis

The flow of molten steel in the actual tundish is very complicated, and the high-temperature working environment makes experimentation and measurement extremely difficult. In order to facilitate the study of the flow phenomenon in the tundish, this study has the following assumptions:

(1) The flow of molten steel in the tundish is a steady-state incompressible viscous fluid.
(2) The inclusions are spherical particles, and the movements are independent of each other.
(3) The effect of temperature on flow, density, and viscosity is negligible.
(4) In order to make the flow of molten steel in tundish close to the real situation, the movement of molten steel is turbulent motion.

### Model Formulation

The flow of molten steel in the continuous casting tundish is a three-dimensional turbulent flow, and the mass equation, momentum equation, energy equation, and turbulent kinetic energy equation used in the calculation are as follows.

Continuity equation:

$$\frac{\partial P}{\partial t} + \frac{\partial (\rho \mu_i)}{\partial x_i} = 0 \tag{1}$$

Momentum equation:

$$\frac{\partial (\rho \mu_i \mu_j)}{\partial x_j} = -\frac{\partial P}{\partial x_j} + \frac{\partial}{\partial x_j}\left(\mu_{\text{eff}}\frac{\partial \mu_i}{\partial x_j}\right) + \frac{\partial}{\partial x_i}\left(\mu_{\text{eff}}\frac{\partial \mu_j}{\partial x_i}\right) + \rho g_i \tag{2}$$

Standard $k$–$\varepsilon$ equation describing the turbulent viscosity coefficient (the model can be used to calculate the complicated turbulent flow):

$$\frac{\partial (\rho \mu_i)}{\partial x_i} = \frac{\partial}{\partial x_i}\left[\left(\mu_{\text{eff}} + \frac{\mu_t}{\sigma_k}\right)\frac{\partial k}{\partial x_i}\right] + G - \rho \varepsilon \tag{3}$$

$$\frac{\partial (\rho \mu_i \varepsilon)}{\partial x_i} = \frac{\partial}{\partial x_i}\left[\left(\mu_{\text{eff}} + \frac{\mu_t}{\sigma_\varepsilon}\right)\frac{\partial \varepsilon}{\partial x_i}\right] + c_1\frac{\varepsilon}{k}G - c_2\frac{\varepsilon^2}{k}\rho \tag{4}$$

among them: $G = \mu_t \frac{\partial \mu_j}{\partial x_i}\left(\frac{\partial \mu_j}{\partial x_j} + \frac{\partial \mu_j}{\partial x_j}\right)$; $\mu_{\text{eff}} = \mu + \mu_t = \mu + c_\mu \rho \frac{k^2}{\varepsilon}$.

Energy equation related to temperature field calculation:

$$\rho\left(\frac{\partial T}{\partial t} + C_{\text{p}}\frac{\partial T}{\partial x_i}\right) = \frac{\partial}{\partial x_i}\left(k_{\text{eff}}\frac{\partial T}{\partial x_i}\right) \tag{5}$$

Equation of transport behavior of inclusions in tundish:

$$\frac{du_{\text{pi}}}{dt} = \frac{18u}{\rho_{\text{p}}d_{\text{p}}^2} \cdot \frac{C_{\text{D}}\text{Re}}{24}(u_i - u_{\text{pi}}) + \frac{(\rho_{\text{p}} - \rho)}{\rho_{\text{p}}}g_{\text{p}} + F_i \tag{6}$$

Mass transfer equation of tracer in tundish:

$$\left(\frac{\partial C}{\partial t} + \nabla \times U_{\text{c}}\right) = \nabla \times \left(\rho D_{\text{c}} + \frac{\mu_t}{\text{Sc}_t}\right)\nabla \times \left(\frac{C}{\rho}\right) + S_{\text{C}} \tag{7}$$

where $\rho$ is the density, kg m$^{-3}$; $u_i$ and $u_j$ are the velocity of molten steel in the $i$ and $j$ directions, m s$^{-1}$; $p$ is the pressure, Pa; $\mu_{\text{eff}}$ is the effective viscosity, kg m$^{-1}$ S$^{-1}$; $C_1, C_2, C_\mu, C_k,$ and $C_\varepsilon$ are empirical constants; their values are 1.44, 1.93, 0.99, 1.0, and 1.3, respectively; $k_{\text{eff}}$ is the effective thermal conductivity, W m$^{-1}$ K$^{-1}$; $\rho_{\text{p}}$ is the particle density, kg m$^{-3}$; $d_{\text{p}}$ is the particle diameter, m; $u_{\text{pi}}$ is the particle velocity, m s$^{-1}$; $C_{\text{D}}$ is the drag coefficient; Re is the relative Reynolds coefficient; $F_i$ is the force, N; $S_{\text{c}}$ is the volume source phase, is the residual mass per unit volume of the tracer unit time, kg/(m$^3$ s); and $D_{\text{c}}$ is the tracer diffusion coefficient; this paper takes

$1.1 \times 10^{-8}$ m$^2$/s; $\mu_t$ is the turbulent viscosity of molten steel, kg/(m s); SC$_t$ is the turbulent Schmidt number of the tracer, taken 0.9.

## *Boundary Conditions*

This study defines the ladle shroud as the velocity inlet and assumes that the velocity profile on the inlet section is the same; the outlet is the pressure outlet; the liquid–solid interface is considered to have no slip boundary, the velocity value on the solid wall is 0; the free surface is zero shear stress. The heat radiation loss of the wall and the free surface is neglected; the inclusion particles are adsorbed and removed by the molten steel surface slag layer; the inclusions in contact with the wall surface of the intermediate tundish are considered to be completely rebounded. The simulation parameters involved in the numerical simulation calculation are shown in Table 1.

## Simulation Scheme

The tundish studied in this paper has retaining wall and dam. In the simulation process, the immersion depth of the long nozzle is 300 mm, the working liquid level is 1300 mm, the distance between the long nozzle and the wall is 500 mm, the distance from the outlet to the wall is 450 mm, the distance between the two nozzles is 3990 mm, the distance from the center of the retaining wall to the center of the long nozzle is 1300 mm, the distance from the bottom of the tundish is 500 mm, the distance from the center of the retaining wall to the center of the retaining wall is 700 mm, the height of the dam is 650 mm, and the thickness of the retaining wall is 100 mm. The original tundish and its flow control device are shown in Fig. 1.

In this paper, four kinds of turbulence inhibitors with different geometries are considered, as shown in Fig. 2. The adjustment of flow control device in tundish

Table 1  Important physical parameters for simulation of fluid flow in tundish

| Parameters | Values | Parameters | Values |
|---|---|---|---|
| Viscosity | 0.0067 kg m$^{-1}$ s$^{-1}$ | Thermal conductivity | 41 W m$^{-2}$ K$^{-1}$ |
| Specific heat | 750 J kg$^{-1}$ K$^{-1}$ | Free surface heat flow | 15 kW m$^{-2}$ |
| Density | 7020 kg m$^{-3}$ | Bottom wall heat loss | 1.4 kW m$^{-2}$ |
| Turbulent kinetic energy at the inlet | 0.01V$_{in}^2$ m$^2$/s$^2$ | Long wall heat loss | 3.8 kW m$^{-2}$ |
| Dissipation rate at the inlet | 33.33K$_{in}^{1.5}$ m$^2$/s$^3$ | Short wall heat loss | 3.2 kW m$^{-2}$ |
| Inlet temperature | 1823 K | Inlet diameter | 160 mm |
| Inlet velocity | 0.744 m/s | Tracer diffusion coefficient | $1.1 \times 10^{-8}$ m$^2$/s |
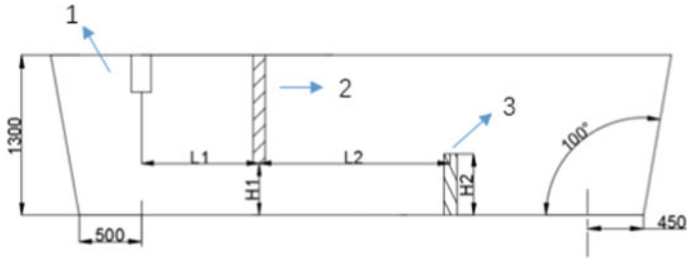
1-Long nozzle:2-Retaining wall:3-Retaining dam

**Fig. 1** Diagram of original tundish. (Color figure online)
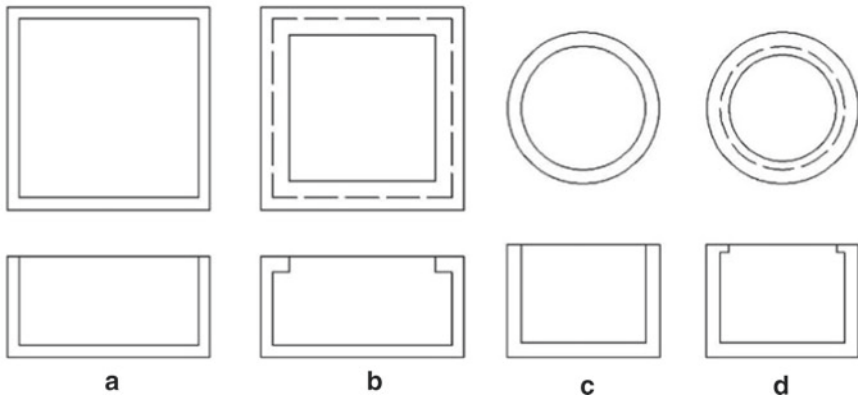


**Fig. 2** Four kinds of turbulence inhibitors

should help to form obvious dense mixing area, can increase the average residence time of molten steel in tundish, control the renewal rate of molten steel, and provide time for inclusion floating. In addition, it will affect the improvement of ingot structure and the reduction of impurities in the produced steel.

## Results and Discussion

Through the simulation of the original tundish (case 0) and the tundish with four different turbulence inhibitors added, the predicted values of flow field, temperature field and inclusion trajectory in the tundish under each scheme were obtained.

## *Comparison of Flow Fields*

Figure 3 shows the velocity vector characteristic diagram of molten steel on the symmetry plane in the tundish under each scheme.

In the tundish with turbulence inhibitors, the first thing to pay attention to is the injection area at the inlet. In the original tundish shown in Fig. 3a, the fluid flows at high speed all the way down to the bottom of the tundish, forming a high negative velocity gradient upward. In the upper left of these high-speed vectors, a large recirculation flow with a smaller velocity is found. The molten steel flows into the tundish from the nozzle, collides with the bottom of the tundish, and then hits the retaining wall and dam to the right. A part of the molten steel flows along the bottom of the tundish to the dam, forming a small backflow near the dam. It can be seen from Fig. 3b–e that the number of reflux in the injection zone is significantly increased, which is conducive to the full mixing of molten steel in the injection zone, improving the mixing degree of molten steel, and playing an important role in improving the quality of molten steel and improving the removal rate of inclusions. The stirring degree of B and C is similar to that of A. D has a small reflux near the liquid surface in the upper right part of the injection zone, and the velocity vector density decreases.

Figure 4 shows the velocity nephogram of liquid level under each scheme. It can be seen that except case A, the areas with higher velocity are in the injection zone.



Velocity Magnitude: 0.2 0.4 0.6 0.8 1 1.2 1.4 1.6 1.8 2 2.2 2.4 2.6
（a）case 0

Velocity Magnitude: 0.2 0.4 0.6 0.8 1 1.2 1.4 1.6 1.8 2 2.2 2.4 2.6
（b）A

Velocity Magnitude: 0.2 0.4 0.6 0.8 1 1.2 1.4 1.6 1.8 2 2.2 2.4 2.6
（c）B

Velocity Magnitude: 0.2 0.4 0.6 0.8 1 1.2 1.4 1.6 1.8 2 2.2 2.4 2.6
（d）C

Velocity Magnitude: 0.2 0.4 0.6 0.8 1 1.2 1.4 1.6 1.8 2 2.2 2.4 2.6
（e）D
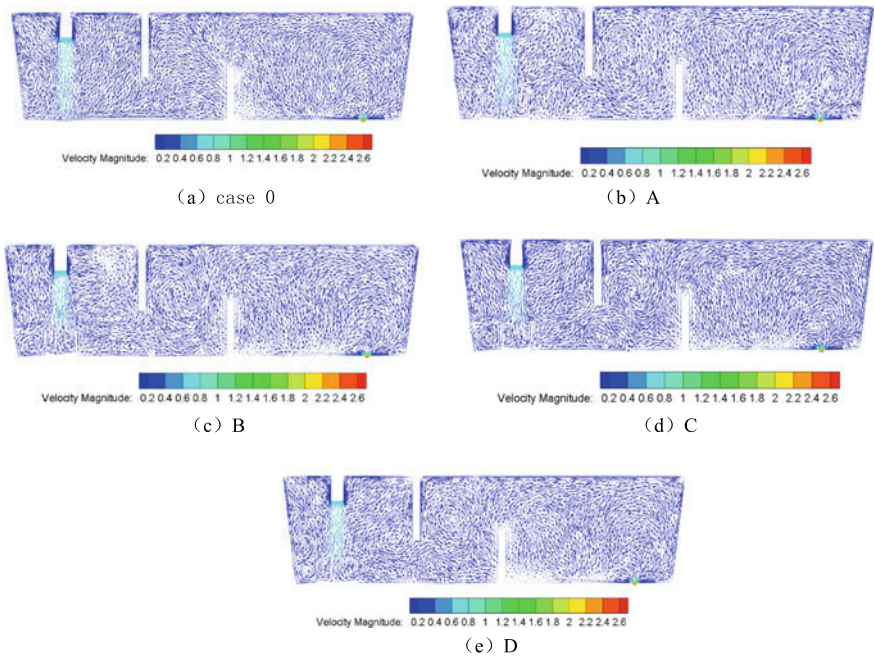
**Fig. 3** Velocity vector diagram of symmetry plane. (Color figure online)

（a）case 0



（b）A



（c）B



（d）C



（e）D
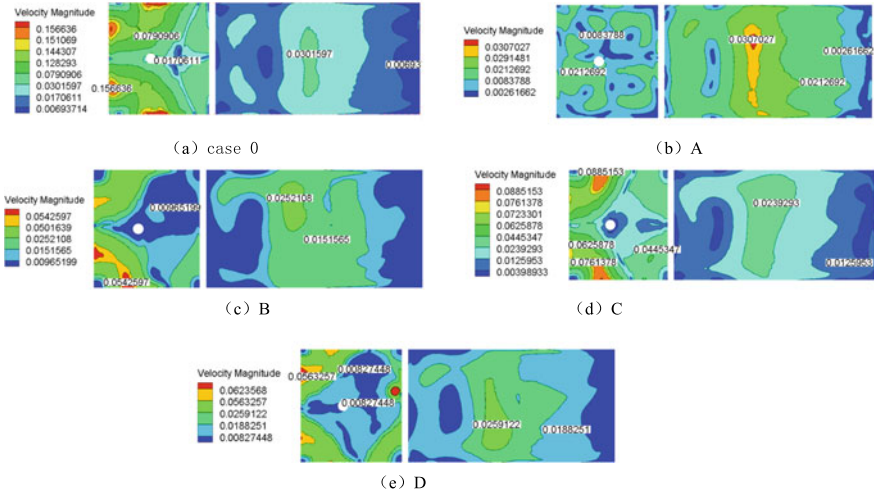
**Fig. 4** Nephogram of velocity distribution of free surface. (Color figure online)

**Table 2** Scheme A-D: free surface velocity

| Scheme | Average velocity of free surface (m/s) |
|--------|-----------------------------------------|
| A | 0.013082756 |
| B | 0.015983118 |
| C | 0.022407318 |
| D | 0.017380551 |

The free surface velocity of the original tundish without turbulence inhibitor is much higher than that of the schemes with turbulence inhibitor. The overall free surface velocity of scheme A is the lowest, the difference between scheme B and scheme D is not much, and the free surface velocity of scheme C is larger than that of other schemes. Table 2 shows the average free surface velocity values of A-D scheme.

## Comparison of Temperature Fields

The temperature field distribution of symmetrical surface of tundish under each scheme is shown in Fig. 5. It can be seen that the temperature distribution of the symmetry surface of the original tundish and the tundish under various schemes can be seen. Combined with Table 3, it can be found that the minimum temperature in the tundish mostly occurs in the dead zone at the upper right corner. It can be seen that the addition of turbulence suppressor is beneficial to the uniform temperature distribution in the left injection zone. On the whole, the effect of turbulence inhibitor on the temperature difference between left and right sides is not obvious.

(a) case 0                                              (b) A

(c) B                                                   (d) C

(e) D
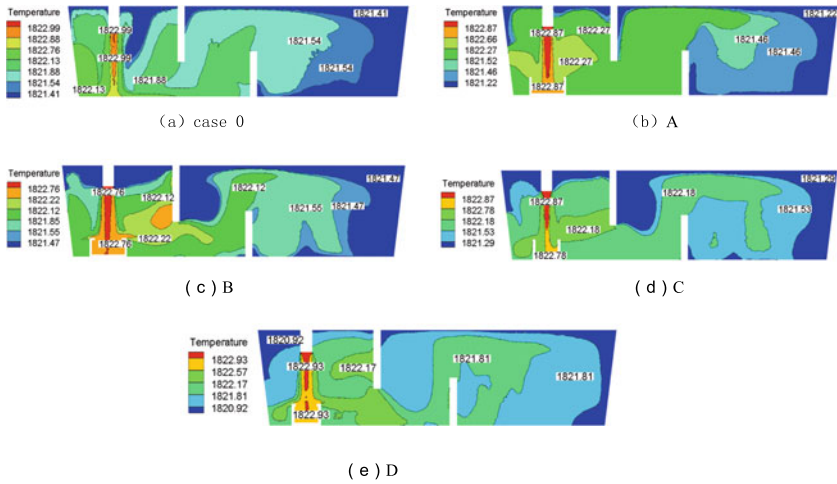
**Fig. 5** Temperature distribution nephogram of symmetry plane. (Color figure online)

**Table 3** Temperature in tundish

| Scheme | Maximum temperature in tundish (°C) | Minimum temperature in tundish (°C) |
|--------|-------------------------------------|-------------------------------------|
| Case 0 | 1823.52 | 1794.55 |
| A | 1823.03 | 1774.06 |
| B | 1823.13 | 1787.10 |
| C | 1824.10 | 1792.20 |
| D | 1823.07 | 1789.99 |

## Comparison of Inclusion Removal Effects

After the calculation by Fluent, the DPM model was used to simulate the inclusion with certain particle size and density added from the long nozzle, and the free surface boundary condition was set as tarp. The inclusion removal rate can be calculated by dividing the captured particles by the total number, as shown in Table 4. It can be seen that the removal rate of inclusions in scheme B and scheme D is relatively high.

**Table 4** Inclusion removal rate

| Scheme | Inclusion removal rate (%) |
|--------|----------------------------|
| Case 0 | 67.5 |
| A | 75.5 |
| B | 78.3 |
| C | 77.8 |
| D | 79.4 |

**Fig. 6** RTD curve. (Color figure online)
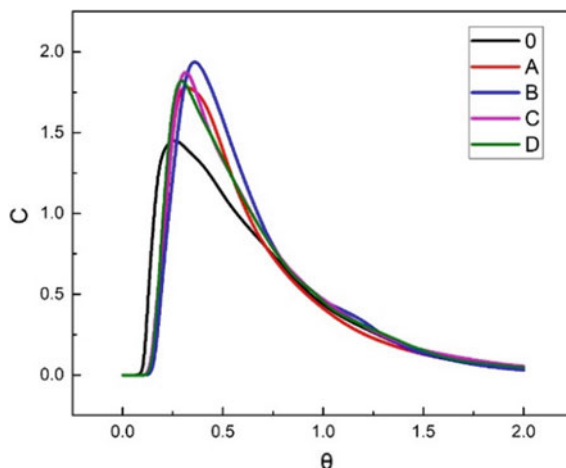


## RTD Curve

The concentration of tracer in tundish with time was calculated by component transfer equation, and the RTD curves under different schemes were obtained. It can be seen from Fig. 6 that the peak value of the original tundish curve is on the left and the peak value is low, and the smoothness degree of other curves is similar. The peak value of curve corresponding to scheme B is right, which indicates that the residence time of molten steel in tundish is increased.

## Conclusions

Through the above analysis of the simulation results, compared with the original tundish, the following conclusions can be drawn for other schemes:

(1) The addition of turbulence inhibitor can make the molten steel fully agitated after entering into the injection zone, make the molten steel well mixed, and increase the probability of inclusion floating.
(2) The maximum velocity of free surface in scheme a is the smallest, followed by BD, and scheme C is larger, but both are smaller and more uniform than the original tundish.
(3) The temperature distribution in the injection region has been improved obviously, but the turbulence suppressor has little effect on the temperature difference between the inlet and outlet regions.
(4) The removal rate of inclusions has been improved obviously, and B and D schemes are the best.

(5) The RTD curve has obvious changes, which indirectly reflects the residence
    time of molten steel in tundish. The peak value is generally increased and right,
    and the peak value of scheme B is the most right.

# References

1. Sun H-b, Zhang J-q (2014) Effect of actual cooling rate of ladle stream on persistent metallurgical performance of a given tundish. J Iron Steel Res (Int) 21(10):915–922
2. Chen D, Xie X, Long M (2014) Hydraulics and mathematics simulation on the weir and gas curtain in tundish of ultrathick slab continuous casting. Metall Mater Trans B 45B(2):392–398
3. Chen C, Cheng G, Zhang J et al (2012) Effects of salt tracer amount, concentration and kind on the fluid flow behavior in a hydrodynamic model of continuous casting tundish. Steel Res Int 83(12):1141–1151
4. Ding N, Bao Y-p, Sun Q-s et al (2011) Optimization of flow control devices in a single-strand slab continuous casting tundish. Int J Miner Metall Mater 18(3):292–296
5. He F, Zhang L-y, Xu Q-Y (2016) Optimization of flow control devices for a T-type five-strand billet caster tundish: water modeling and numerical simulation. China Foundry 03:166–175
6. Yang B, Lei H, Zhao Y et al (2019) Quasi-symmetric transfer behavior in an asymmetric two-strand tundish with different turbulence inhibitor. Metals 9(8)
7. Merder T (2013) The influence of the shape of turbulence inhibitors on the hydrodynamic conditions occurring in a tundish. Arch Metall Mater 58(4):1111–1117

# X-Ray and Neutron Radiographic Experiments on Particle-Laden Molten Metal Flows

**Tobias Lappan, Mārtiņš Sarma, Sascha Heitkam, David Mannes, Pavel Trtik, Natalia Shevchenko, Kerstin Eckert, and Sven Eckert**

**Abstract** In metallurgical processing, non-metallic inclusions contaminating metallic materials are one highly relevant challenge. Bubble injection into molten metals boosts the inclusion control and removal, thus enhancing metal homogenisation and purification. Although this principle of bubble flotation has been used for a long time, the effects of bubble–inclusion interactions in molten metals are not yet well researched. Imaging measurements of multiphase metal flows are challenging for two main reasons: the metals' high melting temperatures and their opaqueness for visible light. This work focuses on X-ray and neutron radiographic experiments employing low-melting gallium alloys laden with model particles smaller than 1 mm in diameter. Both, bubbles and particles, are visualised simultaneously with high spatial and temporal resolution in order to analyse their motions by tracking algorithms. We demonstrate the capability of time-resolved X-ray and neutron radiography to image multiphase flows in particle-laden and optically opaque liquid metals, thus contributing to pave the way for systematic investigations on bubble–inclusion interactions in molten metals.

**Keywords** X-ray radiography · Neutron radiography · Non-metallic inclusions · Liquid metal · Bubble flotation

T. Lappan (✉) · M. Sarma · S. Heitkam · N. Shevchenko · K. Eckert · S. Eckert (✉)
Institute of Fluid Dynamics, Helmholtz-Zentrum Dresden-Rossendorf, Bautzner Landstr. 400, 01328 Dresden, Germany
e-mail: t.lappan@hzdr.de

S. Eckert
e-mail: s.eckert@hzdr.de

S. Heitkam · K. Eckert
Institute of Process Engineering and Environmental Technology, Technische Universität Dresden, 01062 Dresden, Germany

D. Mannes · P. Trtik
Laboratory for Neutron Scattering and Imaging, Paul Scherrer Institut, 5232 Villigen PSI, Switzerland

## Introduction

In aluminium- and steelmaking, the molten metals and alloys get contaminated with inorganic non-metallic inclusions, which typically have inclusion size distributions of the order of 0.01–0.1 mm [1, 2]. Incorporated into the solidified microstructures, such solid inclusions act as three-dimensional defects, affecting the materials' formability and fatigue behaviour.

To control inclusion size distributions and to remove inclusions from molten metals, metallurgical processing employs the principle of bubble flotation [3]. Injecting gas into the molten metal, bubble swarms provide turbulent shear flow, which drives collisions and agglomerations of small inclusions, speeding up the buoyancy-driven removal of larger agglomerates. Additionally, large inclusions are more likely to collide with and attach to bubbles in turbulent flows [4, 5].

For inclusion removal in steel refining, a simple mathematical model predicts an optimum bubble size of 1–5 mm [3]. Flow simulations have quantified collision rates for 0.01 mm aluminium oxide inclusions around a single bubble of 1.4 mm in diameter rising in molten steel [6]. Collision simulations at the inclusion scale show a strong influence of short-distance hydrodynamic effects, particularly when the size ratio of the interacting inclusions is far from unity [7]. Multiscale simulations of an industrial-type gas-stirred steel ladle highlight that steel cleanliness is mainly ruled by agglomeration of the non-metallic inclusions [8], stressing their size ratio as the prevalent parameter [9].

To validate models and simulations, experimental measurement data on bubble–inclusion interactions are lacking. Imaging measurements of multiphase flows in molten metals are challenging for two main reasons: the metals' high melting temperatures and their opaqueness for visible light. Instead, specialised imaging techniques use X-rays or neutrons to gain visual insight into liquid gallium-based alloys at room temperature. In terms of the surface tension and the dynamic viscosity, the eutectic gallium–indium–tin alloy (GaInSn) is comparable to liquid aluminium and liquid iron (Table 1).

**Table 1** Material characteristics of water ($H_2O$) [10] compared to the eutectic gallium–indium–tin alloy (GaInSn) [11], pure gallium (Ga), aluminium (Al), and iron (Fe) [12–14]: melting temperature $T_m$, mass density $\rho_l$, surface tension $\sigma_{lg}$, and dynamic viscosity $\eta_l$

| Material | $T_m$ (°C) | $\rho_l$ (g cm$^{-3}$) | $\sigma_{lg}$ (mN m$^{-1}$) | $\eta_l$ (mPa s) |
|----------|-----------|------------------------|------------------------------|------------------|
| $H_2O$   | 0         | 1.0                    | 73                           | 1.0              |
| GaInSn   | 11        | 6.4                    | 590                          | 2.1              |
| Ga       | 30        | 6.2                    | 720                          | 2.0              |
| Al       | 660       | 2.4                    | 1050                         | 1.4              |
| Fe       | 1538      | 7.0                    | 1880                         | 5.6              |

The properties of water are given at room temperature ($T = 20$ °C), those of the liquid metals at their respective $T_m$

X-ray radiography (XR) has been validated for the characterisation of argon bubbles rising in liquid GaInSn alloy [15]. The effects of bubble coalescence [16] and bubble breakup [17] as well as the influence of a horizontal magnetic field [18] have been investigated in bubble chain experiments. Bubble flows injected through a top submerged lance into liquid GaInSn alloy have been visualised in a recent experimental study [19].

Neutron radiography (NR) has provided insight into single-phase [20, 21] and two-phase flows in the liquid eutectic lead–bismuth alloy [22]. In liquid gallium experiments, NR has imaged rising bubbles under the influence of an electromagnetically driven flow [23] and bubble shape dynamics in samples of representative thickness with and without the application of an external horizontal magnetic field [24, 25]. Further, NR has been employed to study particle motions in an intense liquid gallium flow [26–28] and to observe particle trapping during directional solidification of liquid tin [29].

In addition to radiographic measurements in liquid metals, both XR and NR have proven useful for flow visualisation in optically opaque liquid foam and froth [30, 31], especially in combination with custom-tailored tracer particles [32].

This work employs X-ray radiography as well as neutron radiography to visualise and measure multiphase flows of both gas bubbles and solid particles in low-melting gallium-based alloys at room temperature. Two different types of flow experiments are investigated: first, bubbles rising in particle-laden liquid metal, and second, particle-laden liquid metal flow around a fixed cylindrical obstacle, which is motivated by a single rising bubble. In particular, the radiographic measurements focus on suitable particles of smallest possible diameter that can be imaged in liquid metals using either X-ray or neutron radiation. Such model particles of less than 1.0 mm in diameter – preferably even smaller than 0.1 mm – are the basis to further investigate effects on bubble–inclusion interactions in molten metals by means of radiographic model experiments.

## Experimental Setup

### *Bubble Column*

The experiments on rising bubbles are performed in a flat cuvette-like container (Fig. 1) filled with the liquid metal and the respective model particles for either X-ray radiography or neutron radiography. Made from acrylic glass, the container is resistant to gallium-based alloys as well as to X-ray and neutron radiation. Because acrylic glass is opaque to neutrons, the front and back window can be replaced by soda lime glass plates. The container's inner cross-section measures 70 mm in width, but only 3 mm in depth, along the X-ray or neutron beam direction. This limited thickness results from the attenuation characteristics of the multiphase system. To generate a reproducible bubble chain, argon gas is injected continuously through a
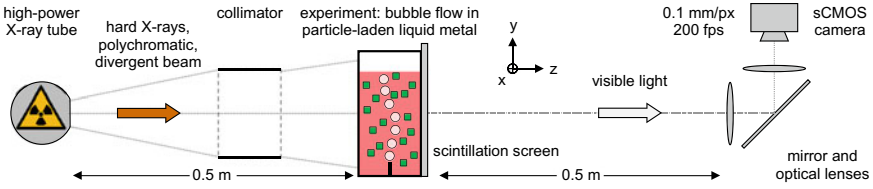
**Fig. 1** Experimental arrangement for X-ray radiography of bubble flows in particle-laden liquid metals: the divergent X-ray beam penetrates the liquid metal experiment placed between the high-power X-ray tube and the X-ray image detection system. (Color figure online)

stainless steel hollow needle with 0.4 mm outer diameter, controlled by a digital mass flow controller (type 1179B, MKS Instruments). After detachment from the faceted needle tip, which is centred 10 mm above the container bottom and 105 mm below the filling level, the bubbles ascend to the free surface of the particle-laden liquid metal. In order to concentrate the particles near the needle tip and, hence, to increase the probability of particle interactions with the detaching bubbles, the width of rectangular cross-section tapers in the lower part of the bubble column. Both the bubbles' and particles' trajectories are visualised and measured within the liquid metal volume above the nozzle tip.

For X-ray radiography, the ternary eutectic gallium–indium–tin alloy (GaInSn, mass fractions: $w_{Ga} = 0.670$, $w_{In} = 0.205$, $w_{Sn} = 0.125$) [11] serves as the model liquid metal. For neutron radiography, this work employs liquid gallium alloyed with tin (GaSn: $w_{Ga} = 0.93$, $w_{Sn} = 0.07$). The chemical composition is close to the system's eutectic point ($w_{Sn} = 0.12$) at $T_{m,GaSn} = 21$ °C [33]. Because the tin content is low, the binary GaSn alloy is assumed to resemble pure gallium rather than the ternary GaInSn alloy in terms of surface tension and dynamic viscosity (cf. Table 1).

Setting the argon gas flow rate to 10 sccm, the bubble chain detaches from the needle with a frequency of approximately 20 bubbles per second, yielding the bubbles' Sauter mean diameter $d_b = 2.5$ mm. For the given bubble diameter and material parameters, Grace's bubble shape diagram [34] predicts the transition between spherical and wobbling shapes in unhindered gravitational motion. However, the 3-mm-thin container confines the comparatively large bubbles: X-ray radiographic experiments reveal effects of flow confinement on bubble shape dynamics [35].

## *Liquid Metal Loop*

The experiments on the particle-laden liquid metal flow around a fixed cylindrical obstacle are performed in a flat channel constructed as a closed circuit. The channel's rectangular cross-section measures 30 mm in width and, in agreement with the bubble column, 3 mm in depth. Motivated by a single rising bubble, a rigid cylinder of 5 mm in diameter is fixed in the centre of the straight channel section. The liquid metal loop is equipped with a disc-type electromagnetic induction pump to drive the flow. Contrary to the bubble column, the liquid metal loop is exclusively used for

neutron radiographic experiments, employing the liquid GaSn alloy with gadolinium oxide particles. Further details on the experimental setup with the electromagnetic induction pump as well as on the particle dispersion procedure are described in [36].

## Model Particles

For X-ray radiography in the liquid GaInSn alloy, model particles based on lead (Pb) or tungsten (W) are employed, because these heavy metals have high X-ray attenuation coefficients. The contrast-to-noise ratio $CNR_X$ is measured for static lead–tin spheres (Pb90Sn10) of 0.1–0.9 mm in diameter and tungsten carbide – cobalt spheres (WC–Co) of 0.6–0.8 mm in diameter. The bubble flow experiments are performed with either Pb90Sn10 spheres of 0.76 mm in diameter (Fig. 2a) or WC–Co granules larger than 0.71 mm (Fig. 2b).

For neutron radiography in the liquid GaSn alloy, model particles based on gadolinium (Gd) are employed, because this rare-earth metal has an outstandingly high neutron attenuation coefficient $\mu_{n,Gd} = 1.5 \times 10^3$ cm$^{-1}$, compared to the liquid metal $\mu_{n,GaSn} = 0.5$ cm$^{-1}$ [36]. The particles made from either gadolinium or gadolinium oxide (Gd$_2$O$_3$) have an irregular shape with a minimum Feret diameter between 0.3 and 0.5 mm. Both particle materials are tested in bubble flow experiments, but only Gd$_2$O$_3$ particles are used in the liquid metal loop with the electromagnetic induction pump.

The terminal velocity $v_t$ and the Stokes number $St_p$ [37] of different model particles of 0.5 and 0.1 mm in diameter are estimated and listed in Table 2. The terminal velocity characterises the particles' buoyancy-driven motion. The Stokes number expresses how quickly the particles adapt to an accelerated flow field, here induced by a rising argon bubble of 2.5 mm in diameter at 0.28 m s$^{-1}$ terminal rising velocity and bubble Reynolds number $Re_b \approx 2100$. Particles with Stokes numbers $St_p < 1$ have good capabilities to follow the acceleration.
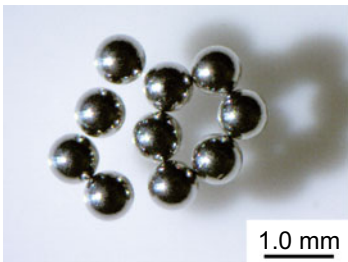


(a) $d_{Pb90Sn10} = 0.76$ mm, spherical shape



(b) $d_{WC-Co} > 0.71$ mm, irregular shape

**Fig. 2** Model particles for X-ray radiographic experiments on particle-laden liquid metal flows: **a** the lead–tin spheres (Pb90Sn10) and **b** the tungsten carbide – cobalt granules (WC–Co) are of a different size and shape; stereo-microscopic images